Monthly Notices
of the
ROYAL ASTRONOMICAL SOCIETY

Mon. Not. R. Astron. Soc. **424,** 830–842 (2012) doi:10.1111/j.1365-2966.2012.21203.x

Axially symmetric pseudo-Newtonian hydrodynamics code

Jinho Kim,[1⋆] Hee Il Kim,[1,2⋆] Matthew William Choptuik[3⋆†] and Hyung Mok Lee[1⋆]

[1]*Department of Physics and Astronomy, FPRD, Seoul National University, Seoul 151-742, Korea*
[2]*Korea Institute of Science and Technology Information, 245 Daehak-ro, Yuseong-gu, Daejeon 305-806, Korea*
[3]*Department of Physics and Astronomy, University of British Columbia, 6224 Agricultural Road, Vancouver, BC V6T 1Z1, Canada*

Accepted 2012 April 26. Received 2012 April 26; in original form 2012 April 12

ABSTRACT

We develop a numerical hydrodynamics code using a pseudo-Newtonian formulation that uses the weak-field approximation for the geometry, and a generalized source term for the Poisson equation that takes into account relativistic effects. The code was designed to treat moderately relativistic systems such as rapidly rotating neutron stars. The hydrodynamic equations are solved using a finite volume method with high-resolution shock-capturing techniques. We implement several different slope limiters for second-order reconstruction schemes and also investigate higher order reconstructions such as the piecewise parabolic method, essentially non-oscillatory method (ENO) and weighted ENO. We use the method of lines to convert the mixed spatial-time partial differential equations into ordinary differential equations (ODEs) that depend only on time. These ODEs are solved using second- and third-order Runge–Kutta methods. The Poisson equation for the gravitational potential is solved with a multigrid method, and to simplify the boundary condition, we use compactified coordinates which map spatial infinity to a finite computational coordinate using a tangent function. In order to confirm the validity of our code, we carry out four different tests including one- and two-dimensional shock tube tests, stationary star tests of both non-rotating and rotating models, and radial oscillation mode tests for spherical stars. In the shock tube tests, the code shows good agreement with analytic solutions which include shocks, rarefaction waves and contact discontinuities. The code is found to be stable and accurate: for example, when solving a stationary stellar model the fractional changes in the maximum density, total mass, and total angular momentum per dynamical time are found to be 3×10^{-6}, 5×10^{-7} and 2×10^{-6}, respectively. We also find that the frequencies of the radial modes obtained by the numerical simulation of the steady-state star agree very well with those obtained by linear analysis.

Key words: gravitation – hydrodynamics – relativistic processes – methods: numerical.

1 INTRODUCTION

It is necessary to take into account both special and general relativistic effects in the studies of the dynamics of compact astrophysical objects such as neutron stars and black holes. Some pulsars produce pulses of up to 1 KHz, corresponding to rotation speeds at the surface of around $0.2c$. Their typical sizes and masses are known to be around 10 km and $1.4 \sim 2\,\mathrm{M}_{\odot}$, respectively, giving compactness, $GM/Rc^2 = 0.2 \sim 0.3$. Therefore, a Newtonian approach cannot properly describe neutron stars, even for the non-rotating case.

In general relativity, the dynamics of gravity (or space–time) can be studied by solving the Einstein equations. The equations of motion for the matter are given, in part, by the conservation law of the energy momentum tensor which itself sources the gravitational field. Computational approaches for solving general relativistic field equations constitute the field of numerical relativity.

Over the past few decades, many general relativistic hydrodynamic codes have been developed, starting with Wilson (1972) who proposed a 3+1 Eulerian formulation (see also Wilson & Mathew 2003). Although Wilson's numerical approach was widely used to study problems such as core collapse and accretion discs, it produced large errors when fluid flows became ultrarelativistic (Centrella & Wilson 1984; Norman & Winkler 1986). In order to avoid these excessive errors, a new formulation was proposed by Marti, Ibanez & Miralles (1991). This formulation makes it possible to use existing numerical techniques based on characteristic approaches for Newtonian hydrodynamics. In particular, these include

⋆E-mail: jinho@astro.snu.ac.kr (JK); khi@astro.snu.ac.kr (HIK); choptuik@phas.ubc.ca (MWC); hmlee@snu.ac.kr (HML)
†Canadian Institute for Advanced Research Cosmology, and Gravity Program Fellow.

high-resolution shock-capturing (HRSC) methods that reduce the order of accuracy near shocks, but minimize the amount of numerical dissipation. This dissipation is very unnatural and can result in non-physical effects in the numerical results. Marti's formulation was extended to the general relativistic case by the Valencia group (Font et al. 2000), and this last work forms the basis for most recent general relativistic hydrodynamical codes. Recent reviews of the formulation and numerical methods can be found in Martí & Müller (2003) and Font (2008).

However, when working in multiple spatial dimensions, it still requires a lot of computational resources to treat fluid dynamics in concert with the evolution of the general relativistic gravitational field. In addition, numerical relativity simulations have frequently encountered instabilities which are often associated with violations of the Hamiltonian and momentum constraints. [However, with the development of new formulations that cast the Einstein equations in appropriate hyperbolic forms, as well as the use of constraint-damping techniques, significant progress has been made on this front: see Sarbach & Tiglio (2012) for a very recent review on this subject.] For these reasons, simulations using Newtonian gravity are still used even though they are not applicable to very compact objects.

The aim of this paper is (1) to introduce a new formulation that applies a pseudo-Newtonian approach (Kim, Kim & Lee 2009) to the study of moderately relativistic objects; and (2) to describe a numerical implementation of this method. In our pseudo-Newtonian approach, which was introduced by Kim et al. (2009) for steady-state models, the gravitational field is treated by a weak-field approximation, but special relativistic effects are correctly taken into account. Specifically, the Newtonian gravitational potential that appears in the weak-field metric satisfies a Poisson equation, but the mass density that appears as a source term for that equation is modified to include relativistic effects. Of course, this method cannot be applied to highly relativistic systems, but Kim et al. (2009) showed that the pseudo-Newtonian formulation is valid for the modelling of mildly compact objects, such as rotating neutron stars having surface rotation velocity up to $\sim 0.2c$ and compactness ~ 0.2 (Kim et al. 2009). In this paper, we extend the pseudo-Newtonian approach to hydrodynamical systems where the flows can be ultrarelativistic and gravity can be moderately strong.

Our method is very efficient in studying dynamics involving moderately relativistic compact objects such as neutron stars because of the relatively small computational resource requirement and accurate calculations with better stability compared to the fully relativistic codes. Possible application areas include: (1) stability of rapidly rotating compact objects; (2) excitation and decay of normal mode oscillations in neutron stars; (3) core collapse of protoneutron stars; and (4) accretion discs around neutron stars and induced jets.

The remainder of this paper is structured as follows. In Section 2, we present the formulation and governing equations for our system, while the numerical techniques employed in our study are given in Section 3. We discuss various numerical tests of our code's treatment of hydrodynamics for the case of shock tubes in Section 4, and for stationary stars in Section 5. A test that compares radial pulsation mode frequencies for polytropic stars determined through dynamical evolution to those computed in linear theory is detailed in Section 6. We conclude with a summary and discussion in Section 7.

Throughout this paper, we use units in which $c = G = \mathrm{M}_\odot = 1$: these correspond to unit time $= 4.92 \times 10^{-3}$ ms, unit length $=$ 1.47 km and unit mass $= 1.99 \times 10^{33}$ g.

2 FORMULATION

Our pseudo-Newtonian method was first discussed in the steady-state context by Kim et al. (2009). We assume the weak-field metric

$$\begin{aligned} \mathrm{d}s^2 &= g_{\mu\nu}\mathrm{d}x^\mu \mathrm{d}x^\nu \\ &= -(1+2\Phi)\,\mathrm{d}t^2 + (1+2\Phi)^{-1}\delta_{ij}\,\mathrm{d}x^i\,\mathrm{d}x^j, \end{aligned} \tag{1}$$

where $g_{\mu\nu}$ is the space–time metric and Φ is the Newtonian gravitational potential. With this metric, we neglect all higher order effects such as frame dragging and describe gravity using only a single gravitational potential, just as in the Newtonian case. The gravitational potential satisfies a Poisson equation with the active mass density, ρ_{active}, providing the source

$$\nabla^2\Phi = 4\pi\rho_{\mathrm{active}}. \tag{2}$$

The active mass density is computed from the relativistic definition of energy. For a perfect fluid, the energy momentum tensor can be expressed as

$$T^{\mu\nu} = \rho_0 h u^\mu u^\nu + P g^{\mu\nu}, \tag{3}$$

where the specific enthalpy is defined by

$$h = 1 + \epsilon + \frac{P}{\rho_0}. \tag{4}$$

The active mass density is then given by

$$\rho_{\mathrm{active}} = T - 2T^0_0 = T^i_i - T^0_0 = \rho_0 h\frac{1+v^2}{1-v^2} + 2P. \tag{5}$$

In equations (3), (4) and (5), ρ_0 is the rest-mass density which is proportional to the number density of baryons of the fluid, P is the pressure, u^μ is the 4-velocity of a fluid element with respect to an Eulerian observer, ϵ is the specific internal energy, T is the trace of the energy momentum tensor ($T = g_{\mu\nu}T^{\mu\nu}$), and v is the three-dimensional fluid velocity. Unlike the Newtonian case, ρ_{active} includes all sources of energy.

The equations governing the motion of the fluid matter can be derived from the conservation laws for the energy momentum tensor and the fluid's matter current, that is, $\nabla_\mu T^{\mu\nu} = 0$ and $\nabla_\mu J^\mu = 0$. In the Arnowitt, Deser & Misner (1962) decomposition of space–time, the metric ($g_{\mu\nu}$) can be expressed in the following form by considering the foliation of space–time using three-dimensional hypersurfaces defined by $t =$ constant:

$$\mathrm{d}s^2 = -\alpha^2\mathrm{d}t^2 + \gamma_{ij}\left(\mathrm{d}x^i + \beta^i\mathrm{d}t\right)\left(\mathrm{d}x^j + \beta^j\mathrm{d}t\right). \tag{6}$$

Here γ_{ij} is the spatial metric, defined on each hypersurface, while α and β^i are known as the lapse and shift vector, respectively, and encode the four-fold coordinate freedom of general relativity.

Flux-conservative formulations of hydrodynamics have been applied very successfully in computational fluid dynamics. To cast the fluid equations in flux-conservative form, we first define so-called conservative variables (q) in terms of the original hydrodynamic variables (so-called primitive variables, w),

$$q = \begin{pmatrix} D \\ S_i \\ \tau \end{pmatrix} = \begin{pmatrix} \rho_0 W \\ \rho_0 h W^2 v_i \\ \rho_0 h W^2 - P - D \end{pmatrix}, \quad w = \begin{pmatrix} \rho_0 \\ v^i \\ P \end{pmatrix}, \tag{7}$$

where $W = 1/\sqrt{1-\gamma_{ij}v^iv^j}$. With these definitions, and with the metric (equation 6), we can then write the Euler equation as (Font et al. 2000)

$$\frac{\partial\left(\sqrt{\gamma}q\right)}{\partial t} + \frac{\partial\left(\sqrt{-g}f^i\right)}{\partial x^i} = \sqrt{-g}\Sigma, \tag{8}$$

where the fluxes f^i and the sources Σ are given by

$$f^i = \begin{bmatrix} D\left(v^i - \frac{\beta^i}{\alpha}\right) \\ S_j\left(v^i - \frac{\beta^i}{\alpha}\right) + P\delta^i_j \\ \tau\left(v^i - \frac{\beta^i}{\alpha}\right) + Pv^i \end{bmatrix},$$
$$\Sigma = \begin{bmatrix} 0 \\ T^{\mu\nu}\left(\partial_\mu g_{\mu j} - \Gamma^\lambda_{\mu\nu} g_{\lambda j}\right) \\ \alpha\left(T^{\mu 0}\partial_\mu(\ln\alpha) - \Gamma^0_{\mu\nu} T^{\mu\nu}\right) \end{bmatrix}. \quad (9)$$

Here $\sqrt{\gamma}$ and $\sqrt{-g}$ are the determinants of γ_{ij} and $g_{\mu\nu}$, respectively, and are related by $\sqrt{-g} = \alpha\sqrt{\gamma}$. It is well known that for a perfect fluid, the system of equations derived from the conservation laws is not closed: the number of dynamical equations is always less than the number of unknowns.

As is also well known, the equation of state (hereafter EoS) for the fluid provides an additional equation, but in the general case it also introduces other unknowns. In order to completely close the hydrodynamical equations, an energy-balance equation is often used. However, under certain circumstances, we can adopt rather simple EoSs that do not introduce any further variables: adiabatic and isothermal EoSs provide specific examples.

Realistic EoSs are usually determined by theoretical calculations and experimental measurements. However, there are physical regimes where our understanding of the nature of the matter is quite incomplete. Specifically, in the case where the matter density is significantly above nucleon density, there remain large uncertainties in the correct EoS. Thus, for example, the EoS at the core of neutron stars is still not very well understood. Here we ignore these difficulties, and for the purpose of testing our code, we use two types of very simple EoS. The first is the ideal gas EoS which can be written in the following form:

$$P = (\Gamma - 1)\,\rho_0\epsilon, \quad (10)$$

and corresponds to the isothermal EoS. We use this EoS in the shock tube tests described in Section 4. The second EoS results from the isentropic assumption, whereby equation (10) becomes the polytropic EoS:

$$P = K\rho_0^{1+\frac{1}{N}}. \quad (11)$$

Here K and N are the polytropic constant and index, respectively. The polytropic EoS is the generalized form of the adiabatic one; a fluid which is governed by it does not generate entropy, and shock formation is thus generically prohibited. We use this EoS in the pulsation mode test (Section 6 and Appendix A).

Using the above formulation, we are now ready to describe in detail the pseudo-Newtonian hydrodynamical equations used in our code. We limit our study here to axisymmetric systems, and adopt cylindrical coordinates (R, Z, ϕ) such that

$$ds^2 = -(1+2\Phi)\,dt^2 + \frac{1}{1+2\Phi}\left(dR^2 + dZ^2 + R^2 d\phi^2\right). \quad (12)$$

The lapse function and shift vector are thus given by $\alpha = \sqrt{1+2\Phi}$ and $\beta^i = 0$, respectively. In addition, we enforce the equatorial symmetry at $z = 0$. In this coordinate system, the conservative and primitive variables are

$$q = \begin{pmatrix} D \\ S_R \\ S_Z \\ S_\phi \\ \tau \end{pmatrix} = \begin{pmatrix} \rho_0 W \\ \rho_0 hW^2 v_R \\ \rho_0 hW^2 v_Z \\ \rho_0 hW^2 v_\phi \\ \rho_0 hW^2 - P - D \end{pmatrix}, \quad w = \begin{pmatrix} \rho_0 \\ v^R \\ v^Z \\ v^\phi \\ P \end{pmatrix}. \quad (13)$$

The final form of the hydrodynamical equations then becomes

$$\frac{\partial\left(\sqrt{\gamma}q\right)}{\partial t} + \frac{\partial\left(\sqrt{-g}f^R\right)}{\partial R} + \frac{\partial\left(\sqrt{-g}f^Z\right)}{\partial Z} = \sqrt{-g}\Sigma, \quad (14)$$

where

$$f^R = \begin{bmatrix} Dv^R \\ S_R v^R + P \\ S_Z v^R \\ S_\phi v^R \\ \tau v^R + Pv^R \end{bmatrix},$$
$$f^Z = \begin{bmatrix} Dv^Z \\ S_R v^Z \\ S_Z v^Z + P \\ S_\phi v^Z \\ \tau v^Z + Pv^Z \end{bmatrix},$$
$$\Sigma = \begin{bmatrix} 0 \\ -\frac{\rho_{\rm active}}{1+2\Phi}\frac{\partial\Phi}{\partial R} + \frac{S_\phi v^\phi}{R} + \frac{P}{R} \\ -\frac{\rho_{\rm active}}{1+2\Phi}\frac{\partial\Phi}{\partial Z} \\ 0 \\ -\left(S_R\frac{\partial\Phi}{\partial R} + S_Z\frac{\partial\Phi}{\partial Z}\right) \end{bmatrix}. \quad (15)$$

Using equation (12) we have $\sqrt{\gamma} = R(1+2\Phi)^{-3/2}$, and $\sqrt{g} = R(1+2\Phi)^{-1}$. In obtaining the expressions in equation (15), we have used the assumption of slow changes of the potential relative to the gradients ($\frac{\partial\Phi}{\partial t} \ll \frac{\partial\Phi}{\partial R}$ or $\frac{\partial\Phi}{\partial Z}$). Recently, Nagakura et al. (2011) used a similar method in the context of jet propagation in a uniform medium, but adopted a slightly different linear momentum equation from ours (see equation 15 and compare with equations 2 and 3 in Nagakura et al. 2011).

Finally, the gravitational Poisson equation in our coordinate system is

$$\frac{1}{R}\frac{\partial}{\partial R}\left(R\frac{\partial\Phi}{\partial R}\right) + \frac{\partial^2\Phi}{\partial Z^2} = 4\pi\rho_{\rm active}. \quad (16)$$

Note that the second component of Σ contains terms which, individually, become singular on the axis of symmetry ($R = 0$). In addition, there are other terms in the equations of motion that need to be treated carefully as $R \to 0$. This is done by demanding regularity at the axis, and by considering the parity of each function, with respect to R, in that limit. In particular, ρ_0, v^Z, v^ϕ, P, D, S_Z, S_ϕ and τ are all even functions of R as $R \to 0$, while v^R and S_R are odd. Taking this into account, equation (14) and Σ in equation (15) become

$$\frac{\partial\left(\sqrt{\gamma'}q\right)}{\partial t} + 2\frac{\partial\left(\sqrt{-g'}f^R\right)}{\partial R} + \frac{\partial\left(\sqrt{-g'}f^Z\right)}{\partial Z} = \sqrt{-g'}\Sigma \quad (17)$$

and

$$\Sigma = \begin{bmatrix} 0 \\ 0 \\ -\frac{\rho_{\rm active}}{1+2\Phi}\frac{\partial\Phi}{\partial Z} \\ 0 \\ -S_Z\frac{\partial\Phi}{\partial Z} \end{bmatrix}, \tag{18}$$

where $\sqrt{\gamma'} = (1+2\Phi)^{-3/2}$ and $\sqrt{-g'} = (1+2\Phi)^{-1}$. The coefficient of $\frac{\partial(\sqrt{-g}f^R)}{\partial R}$ in equation (17) becomes 2 instead of 1, while the other variables, such as q, f^R and f^Z, remain unchanged from equation (15).

Finally, using L'Hopital's theorem at $R = 0$, the singular term $R^{-1}\partial\Phi/\partial R$ in the Poisson equation (16) is replaced by $\partial^2\Phi/\partial R^2$.

3 NUMERICAL METHODS

In this section, we describe our numerical methods for solving the coupled hydrodynamical and Poisson equations. We mainly use a finite volume method for the hydrodynamical equations and a finite difference approach for the Poisson equation. In the finite volume method, each grid cell represents volume-averaged hydrodynamic quantities, that is, $\bar{q} = \frac{1}{\Delta V}\int q\,{\rm d}V$. After applying the finite volume method, our hydrodynamical equations can be reduced to Riemann problems which consider the time-evolution of initial conditions given by two distinct states that adjoin at some interface (so that there are, in general, discontinuities across one or more physical quantities at the interface). A very important property of the finite volume method is that it maintains the local conservation properties of the flow in the computational grid.

In the dynamics of compressible fluids, we inevitably encounter discontinuous behaviours such as shocks, rarefactions or contact discontinuities. To treat such discontinuities without introducing numerical instabilities or spurious oscillations, we use HRSC techniques that generically reduce the order of accuracy of the numerical scheme near discontinuities or when one or more of the fluid variables are at a local maximum. A key ingredient to the success of the HRSC methods is the calculation of fluxes through cell boundaries. To compute these fluxes, we need approximate values for the primitive variables at the cell boundaries. We have implemented second-order slope limiters such as minmod (van Leer 1979), monotonized central difference (hereafter MC, van Leer 1977) and superbee (Roe 1985), as well as a third-order slope limiter proposed by Shibata (2003) and which is based on the minmod function (hereafter 3minmod). Other reconstruction methods such as the third-order piecewise parabolic method (PPM, Colella & Woodward 1984), essentially non-oscillatory method (ENO, Harten et al. 1987) and weighted ENO (WENO, Liu, Osher & Chan 1994; Jiang & Shu 1996), which has an arbitrary order of accuracy, were also implemented.

In the implementation of HRSC schemes, it is not efficient to exactly solve the Riemann problems which arise since an excessively large amount of computational resources per cell are then needed to calculate the fluxes. Thus, an approximate calculation of fluxes is performed. We implemented the following three schemes: Roe (Roe 1981), Marquina (Donat & Marquina 1996; Donat 1998) and HLLE (Harten, Lax & van Leer 1983; Einfeldt 1988; Einfeldt et al. 1991) approximations. The Roe approximation is based on the Rankine–Hugoniot jump condition and Marquina's approach generalizes Roe's scheme. The HLLE algorithm comes from a very simple two-wave approximation and produces the most dissipative and stable results. We have mainly used HLLE for reducing computational cost but found that our results were not significantly influenced by the type of flux approximation used.

In order to solve the Poisson equation (which is elliptic) for the gravitational potential, we use the multigrid method, which can quickly reduce low-frequency error components in the solution by adopting hierarchical grid levels (Brandt 1977). One of the difficulties we often encounter with the Poisson equation is in the proper implementation of the boundary conditions. For example, one of the natural boundary conditions is $\Phi = 0$ at ∞, but in the coordinates adopted in the previous section the computational domain cannot reach spatial infinity. We thus now refer to our previous coordinates as (r, z) and introduce new coordinates (R, Z) which compactify the spatial domain, mapping the infinities in each spatial direction to finite coordinate values. Specifically, we choose the same type of compactification for both r and z coordinates, namely a tangent function, but allow a certain portion of the domain to remain 'uncompactified':

$$r = \begin{cases} R & \text{if } R \le r_0 \\ r_0 + r_1 \tan\left(\frac{R-r_0}{r_1}\right) & \text{if } R > r_0 \end{cases}, \tag{19}$$

$$z = \begin{cases} Z & \text{if } Z \le z_0 \\ z_0 + z_1 \tan\left(\frac{Z-z_0}{z_1}\right) & \text{if } Z > z_0 \end{cases}. \tag{20}$$

Here, the four parameters z_0, z_1, r_0 and r_1 control the compactification, and we chose this specific form for the coordinate transformation since it guarantees that the compactified coordinates smoothly transition to the original ones near the origin. We note that we solve the hydrodynamical and gravitational equations on separate spatial domains: $[0 : r_0, 0 : z_0]$ for the hydrodynamic calculations and $\left[0 : r_0 + \frac{2}{\pi}r_1, 0 : z_0 + \frac{2}{\pi}z_1\right]$ for the computation of the gravitational potential. Their ranges correspond to $[0 : r_0, 0 : z_0]$ and $[0 : \infty, 0 : \infty]$, respectively, in the original cylindrical coordinates (r, z). In the compactified coordinates, the Poisson equation is written as

$$\frac{1}{rf(R)}\frac{\partial}{\partial R}\left(\frac{r}{f(R)}\frac{\partial\Phi(R,Z)}{\partial R}\right) + \frac{1}{g(Z)}\frac{\partial}{\partial Z}\left(\frac{1}{g(Z)}\frac{\partial\Phi(R,Z)}{\partial Z}\right) = 4\pi\rho_{\rm active}, \tag{21}$$

where $f(R)$ and $g(Z)$ are given by

$$f(R) = \frac{{\rm d}r}{{\rm d}R} = \begin{cases} 1 & \text{if } R \le r_0 \\ \sec^2\left(\frac{R-r_0}{r_1}\right) & \text{if } R > r_0, \end{cases} \tag{22}$$

$$g(Z) = \frac{{\rm d}z}{{\rm d}Z} = \begin{cases} 1 & \text{if } Z \le z_0 \\ \sec^2\left(\frac{Z-z_0}{z_1}\right) & \text{if } Z > z_0 \end{cases}. \tag{23}$$

As just noted, the domain for the hydrodynamical calculation is finite, that is, we do not solve the hydrodynamical equations on the full compactified domain, and we thus must be careful to choose values of r_0 and z_0 large enough so that there is no outflux of matter through the $r = r_0$ and/or $z = z_0$ boundaries. In our code, we set $r_0 = z_0 = \eta r_{\rm e}$, where η is a free parameter and $r_{\rm e}$ is the equatorial radius of the rotating star as obtained from the procedure we use to calculate the initial stellar model. For the pulsation mode test described in Section 6, a typical choice is $\eta = 2$. This means that the hydrodynamical computational domain extends twice the distance of the stellar radius in both the R and Z directions: this

choice is found to be sufficient for our study. The values of r_1 and z_1 are automatically determined by requiring the multigrid domain to be two times larger than the size of the hydrodynamic domain in compactified coordinates, that is, $r_1 = \frac{\pi}{2} r_0$ and $z_1 = \frac{\pi}{2} z_0$.

In our multigrid algorithm, we use line relaxation for our basic smoother, whereby all grid point values given by $R =$ constant or $Z =$ constant are updated simultaneously (constant-R and constant-Z sweeps are alternated). We cannot use point-wise relaxation since, as is well known, such a technique is not a good smoother when there is significant anisotropy in the coefficients of the second derivative terms in the elliptic operator being treated. This is the case in our compactified coordinate system, particularly near the domain boundaries. We have used second- and fourth-order finite-difference approximations to the Poisson equation, and these lead to tridiagonal and pentadiagonal linear systems, respectively, that must be solved to implement the line relaxations. We use the routines DGTSV (tridiagonal) and DGBSV (banded/pentadiagonal) from LAPACK to find these solutions.

In order to integrate the discretized hydrodynamical equations, we use the method of lines, transforming our partial differential equations in time and space to ordinary differential equations (ODEs) with respect to time. To solve these ODEs, we then employ second- and third-order Runge–Kutta methods, which are known to have the total variation diminishing property.

4 SHOCK TUBE TESTS

In order to verify the accuracy and convergence of our numerical code, we first carry out rigorous tests using initial configurations having analytic solutions. In this section, we present the results of such tests for the case where there is no self-gravity (i.e. pure hydrodynamics). Another test of the entire code – including our treatment of the gravitational field – is described in the next section.

Shock tube tests are Riemann problems where the initial configuration of the fluid is given by two states having, in general, different densities, pressures and velocities, on the left- and right-hand halves of the tube. Three possible distinct features emerge from the subsequent evolution: a shock, a rarefaction fan, and a contact discontinuity. We carried out one- and two-dimensional numerical simulations with three different parameter sets previously used by Zhang & MacFadyen (2006). These parameters are listed in Table 1, where the superscripts 'R' and 'L' represent the fluid states in the right-hand and left-hand halves, respectively, of the tube.

4.1 One-dimensional test in Cartesian coordinates

We first present the results of our one-dimensional tests. In these tests, we carefully examine how the distinct features predicted by the analytic solutions are reproduced by different methods, and measure the accuracy and convergence rate of the various solutions obtained.

Table 1. Initial values of the physical quantities for the shock tube tests (Riemann problem).

Problem	Γ	$\rho_0^{\rm L}$	$\rho_0^{\rm R}$	$v^{\rm L}$	$v^{\rm R}$	$P^{\rm L}$	$P^{\rm R}$
1	5/3	10.0	1.0	0.0	0.0	13.33	10^{-8}
2	5/3	1.0	1.0	0.0	0.0	1000.0	10^{-2}
3	4/3	1.0	1.0	0.9	0.0	1.0	10.0

In problem 1, the initial discontinuity gives three different types of solutions (shock, rarefaction and contact discontinuity). Fig. 1 shows the results at $t = 0.4$ obtained using four different methods of reconstruction: minmod (top left-hand panel), MC (top right-hand panel), 3minmod (bottom left-hand panel) and PPM (bottom right-hand panel). We observe that the minmod method is quite dissipative, yielding rather smooth solutions that cannot accurately describe the shockwave. We also find that at low resolution the height of the shock is not well reproduced if we use the minmod method. MC and 3minmod give almost similar results, while PPM shows the best behaviour near the shock.

The second test problem (problem 2) is the so-called blast wave test which produces a very sharp and thin shell in density between the shock and contact discontinuity. Generally, numerical codes are not able to perfectly resolve this very thin shell because it can span only a few grid cells, even in very high resolution calculations. None the less, this test provides insight into how well a code can handle such a feature. As shown in Fig. 2, PPM again gives the best results, although it still shows large errors at the shock.

The third problem generates a strong reverse shock but the numerical solution has oscillatory features near the shock front. Generally speaking, the oscillation can be easily damped out if the numerical scheme is significantly dissipative. Numerical dissipation also tends to weaken the sharpness of the discontinuity. In Fig. 3, one can see that the minmod methods, which, as already noted, is the most dissipative of the techniques we use, gives relatively small amplitude oscillations, except near the discontinuity. The more non-dissipative methods describe the shock features well, but produce rather large amplitude oscillatory behaviour.

To quantify the deviation of our numerical results from the analytic solutions, we use the L_1 norm of the errors, defined by $L_1 = \sum_{i=1}^{N} \Delta x_i |q_i - q(x_i)|$, where $q(x_i)$ is the value of the analytic solution at point x_i. We summarize the results in Table 2. The convergence rate ($\log_2 \left[L_1^{2h}/L_1^{h}\right]$) in the table should be close to 1, which corresponds to the first-order nature of the HRSC scheme near the shock where most of the L_1-norm error occurs. However, it can deviate from that value due to the oscillatory features near the shock.

Fig. 4 shows the L_1 norms and convergence rates for each problem when the grid resolution is $N = 512$. Although no single method stands out in our one-dimensional shock tube tests, we conclude from the values of the L_1 error norms and convergence rates that PPM gives the most promising results.

4.2 Two-dimensional test in cylindrical coordinates

Since the cylindrical coordinate system we have adopted is curvilinear, one-dimensional shock tube tests are not sufficient for assessing our code's accuracy and convergence. In Cartesian coordinates, fluxes between cells which have the same state cancel out. For example, if we carry out the shock tube test in the x-direction, then the fluxes in the y- and z-directions are identical in every grid cell, meaning that the net flux is 0. Therefore, one-dimensional shock tube tests performed with codes that use two- or three-dimensional Cartesian coordinates produce exactly the same results as a one-dimensional code. However, in cylindrical coordinates, fluxes do not cancel in this way, but rather are balanced by source terms. This difference may give additional non-physical effects, especially near discontinuities.

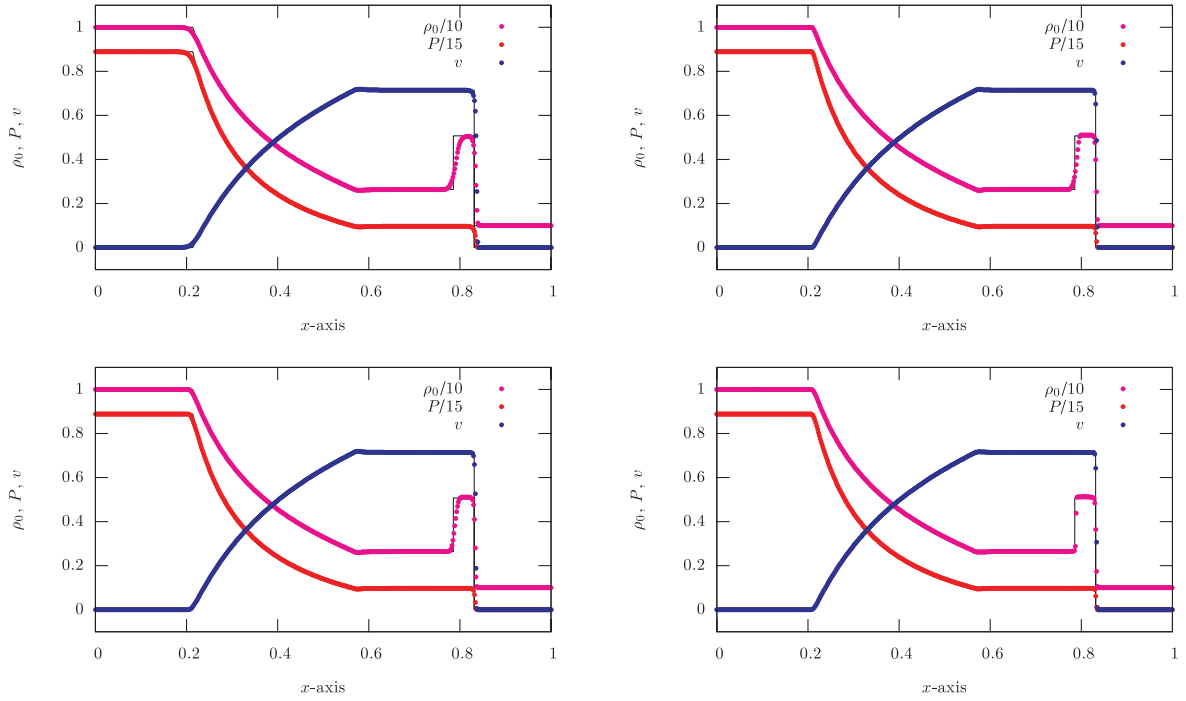

Figure 1. One-dimensional shock tube test of problem 1 at $t = 0.4$ with different reconstruction methods: minmod (top left-hand panel), MC (top right-hand panel), 3minmod (bottom left-hand panel) and PPM (bottom right-hand panel). The initial discontinuity is at $x = 0.5$. We use 512 uniform grid points. The numerical results are shown in three different colours: rest-mass density (pink), pressure (red) and velocity (blue). The solid lines show the analytic solutions.

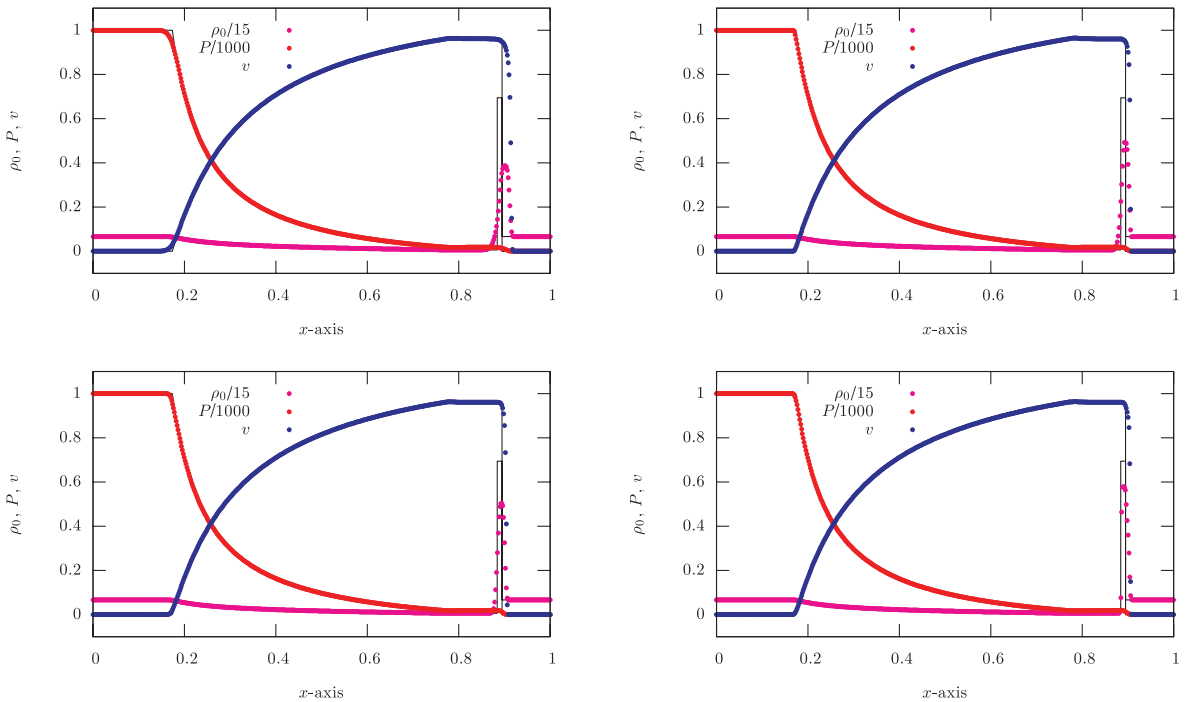

Figure 2. Same as Fig. 1 for problem 2.

Therefore, we carried out the first of the shock tube tests listed in Table 1 in cylindrical coordinates, where we placed the discontinuity on the $Z = 0$ plane. Fig. 5 shows the resulting solution on the Z-axis. If we use the minmod method, the two-dimensional results are similar to the one-dimensional ones. In addition, although PPM produces better results than minmod, it cannot produce the sharp features of the shock seen in the one-dimensional test: this is due to the dissipation caused by the imbalance between the net flux and the source term. We can also see that 3minmod and PPM yield quite similar results. We checked the differences in solutions at different z = constant planes and found that they are negligibly small ($\sim 10^{-13}$) compared to the truncation errors. Overall, however, although the two-dimensional results show more dissipation than the one-dimensional ones, the relative differences in the

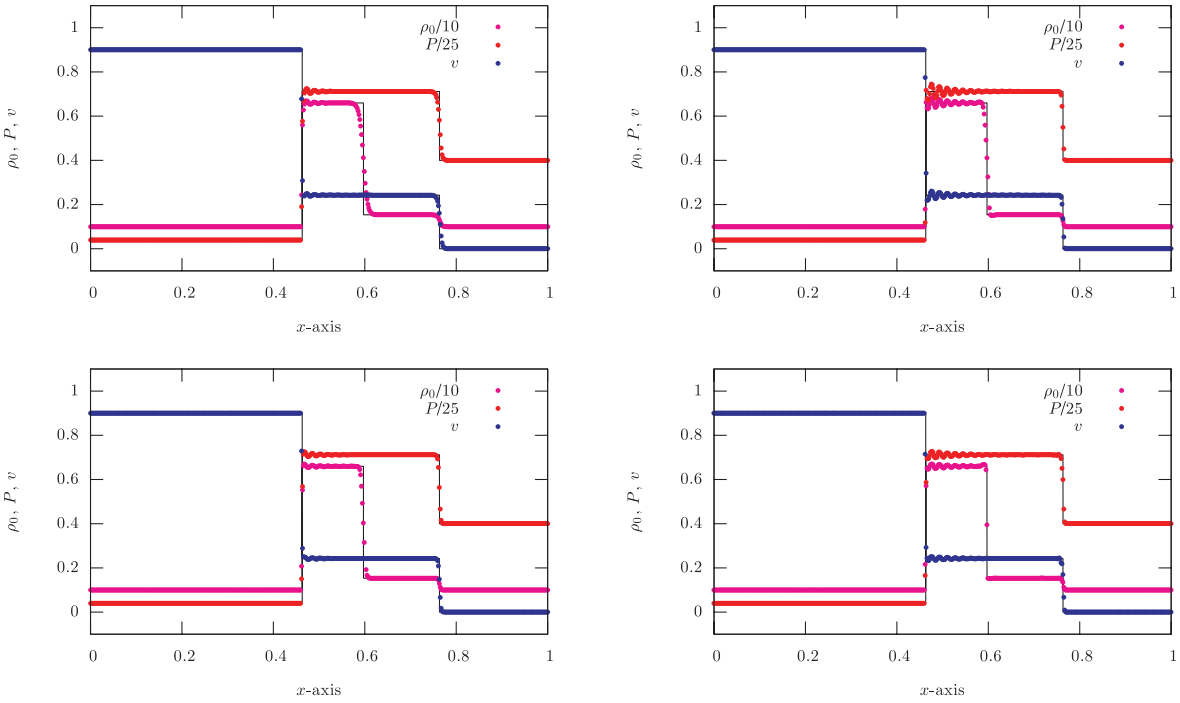

Figure 3. Same as Figs 1 and 2 for problem 3.

Table 2. The L_1 norm of the error and its convergence rate for each of the test problems using different resolutions and different reconstruction schemes.

			N					
			64	128	256	512	1024	2048
Problem 1	minmod	L_1 norm ($\times 10^{-2}$)	25.7	16.5	9.48	5.02	2.66	1.49
		Convergence rate	–	0.64	0.80	0.92	0.91	0.84
	MC	–	15.3	9.43	5.25	2.79	1.46	0.830
		–	–	0.70	0.85	0.91	0.93	0.82
	3minmod	–	17.8	11.0	5.82	2.99	1.51	0.816
		–	–	0.69	0.92	0.96	0.98	0.89
	PPM	–	12.3	6.55	3.43	1.74	0.877	0.431
		–	–	0.91	0.93	0.98	0.99	1.0
Problem 2	–	–	30.1	21.0	20.1	15.8	10.9	6.93
		–	–	0.52	0.061	0.34	0.54	0.65
	–	–	27.8	18.2	14.9	10.4	6.28	3.77
		–	-	0.61	0.29	0.52	0.73	0.74
	–	–	28.3	17.9	13.7	8.84	5.05	2.72
		–	–	0.66	0.39	0.63	0.81	0.89
	–	–	29.5	17.9	12.7	7.79	3.73	2.13
		–	–	0.73	0.49	0.71	1.1	0.81
Problem 3	–	–	15.5	10.0	6.19	3.65	2.37	1.58
		–	–	0.63	0.69	0.76	0.63	0.59
	–	–	14.9	7.73	5.40	2.72	1.64	1.04
		–	–	0.95	0.52	0.99	0.73	0.66
	–	–	13.0	6.97	4.40	2.25	1.35	0.867
		–	–	0.90	0.66	0.97	0.74	0.63
	–	–	7.26	3.93	2.41	1.08	0.547	0.393
		–	–	0.89	0.70	1.16	0.98	0.47

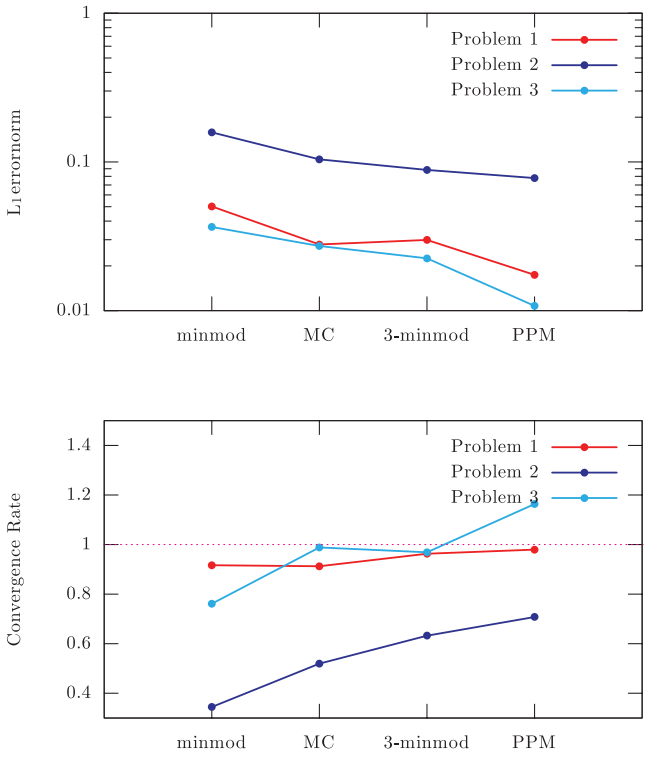

Figure 4. The L_1 norm (top panel) and convergence rate (bottom panel) when the number of grid points is 512 with different reconstruction methods. Three different shock tube problems are shown with different colours (problem 1: blue; problem 2: red; problem 3: sky blue).

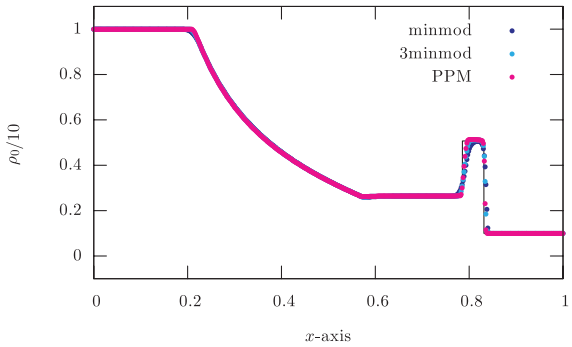

Figure 5. The solution on the axis at $t = 0.4$ in problem 1 in Section 4.1. The three different reconstruction methods (minmod: blue; 3minmod: sky blue; PPM: magenta) are shown.

solutions are not significant (for our purposes). In particular, both agree acceptably with the analytic forms.

5 STATIONARY STAR TEST

The tests just reported did not involve the effects of the gravitational field. In this section, we test our treatment of the Poisson equation for the gravitational potential as well as the hydrodynamics.

With an ideal code, the evolution of a stationary star should also be stationary. However, in practice, all codes that dynamically evolve stationary states show some level of fluctuation due to finite grid resolution and intrinsic errors in the numerical scheme used. In this section, we show the time-evolution of the physical quantities of non-rotating and rotating stars, and investigate the dependence of this time behaviour by changing the resolution of the simulations. Specifically, we use three different grid resolutions: 65×65, 129×129 and 257×257, where half of the grid points span the star at the equator.

Our initial models of rotating stars are generated using Hachisu's self-consistent field (Hachisu 1986a,b) method – details of the procedure are described in Kim et al. (2009). In order to generate equilibrium models, we choose: (1) the maximum rest-mass density, $\rho_0^{\max}$; (2) the rotation parameter, A, which describes the differential rotation; and (3) the axial ratio which determines how fast the star is rotating. We must also specify the EoS in our construction of the initial model. Here, we used the polytropic EoS (31) with $K = 100$ and $N = 1$. We choose a maximum density value of $\rho_0^{\max} = 1.28 \times 10^{-3}$, which, with this EoS, produces a 1.4-$M_\odot$ star in the non-rotating case. For the rotating models, we only consider rigid body rotation, which is obtained when we choose a very large value of A. The axial ratio is specified to be 0.75, resulting in an orbital frequency of 611 Hz.

Even with our use of the multigrid technique – which is generally an efficient method for solving elliptic equations – we find solutions of the Poisson equation for the gravitational potential to be computationally expensive. We thus calculate Φ only every 40 time-steps to reduce the time spent in the Poisson solver, and find that this produces results that are nearly equivalent to those obtained when the Poisson equation is solved at each time-step. However, we use time-extrapolated values for the gravitational potential at the time-steps between solutions of the Poisson equation in order to avoid discontinuities in the primitive variables, when abrupt changes of the gravitational potential occur. We find that these discontinuities give rise to very unnatural dissipative effects in the simulation, resulting, for example, in a rapid decay in the amplitude of radial oscillations, even when radial perturbations are explicitly introduced.

Fig. 6 shows the time-evolution of the relative changes of the maximum density $([\rho_0^{\max}(t) - \rho_0^{\max}(0)]/\rho_0^{\max}(0)$ for non-rotating (left-hand panel) and rigidly rotating (right-hand panel) stars. For the stationary stars, we use the Cowling approximation, which assumes the gravitational potential is fixed. This gives efficient evolution of the stars, and can also be used as a testbed for fully coupled evolutions. The results computed using the Cowling approximation are shown in the top figures. The maximum density slowly increases with time for the rotating star, while it decreases for the non-rotating star. For grid resolutions greater than 65×65, the rate of change is almost independent of resolution for the spherical star, but a slow decrease with resolution is seen for the rotating star. We define the following dimensionless rate of change:

$$\mathcal{R} = \left| t_{\rm dyn} \frac{{\rm d} \ln \rho_0^{\max}}{{\rm d}t} \right|, \tag{24}$$

where we use $t_{\rm dyn} = 1/\sqrt{\rho_0^{\max}}$ for simplicity. We use this quantity – as computed from the highest resolution simulations – as a label in the figures. The values of $\mathcal{R}$ are within 3×10^{-7} for non-rotating stars and are about 10 times larger for rotating stars, again with a maximum resolution of 257×257. The inverse of $\mathcal{R}$ can be interpreted as the time (in units of the dynamical time) for which the simulation can be carried out until the results deviate from the true solution by $O(1)$. Our results indicate that the error would become $\sim$1 per cent in 30 000 and 3000 dynamical times for non-rotating and rotating stars, respectively. We also carried out very long time simulations and found that $\mathcal{R}$ becomes smaller even though it appears to be almost constant in the figures. From these results, we conclude that we can use the code to evolve stellar configurations for several thousand or more dynamical times.

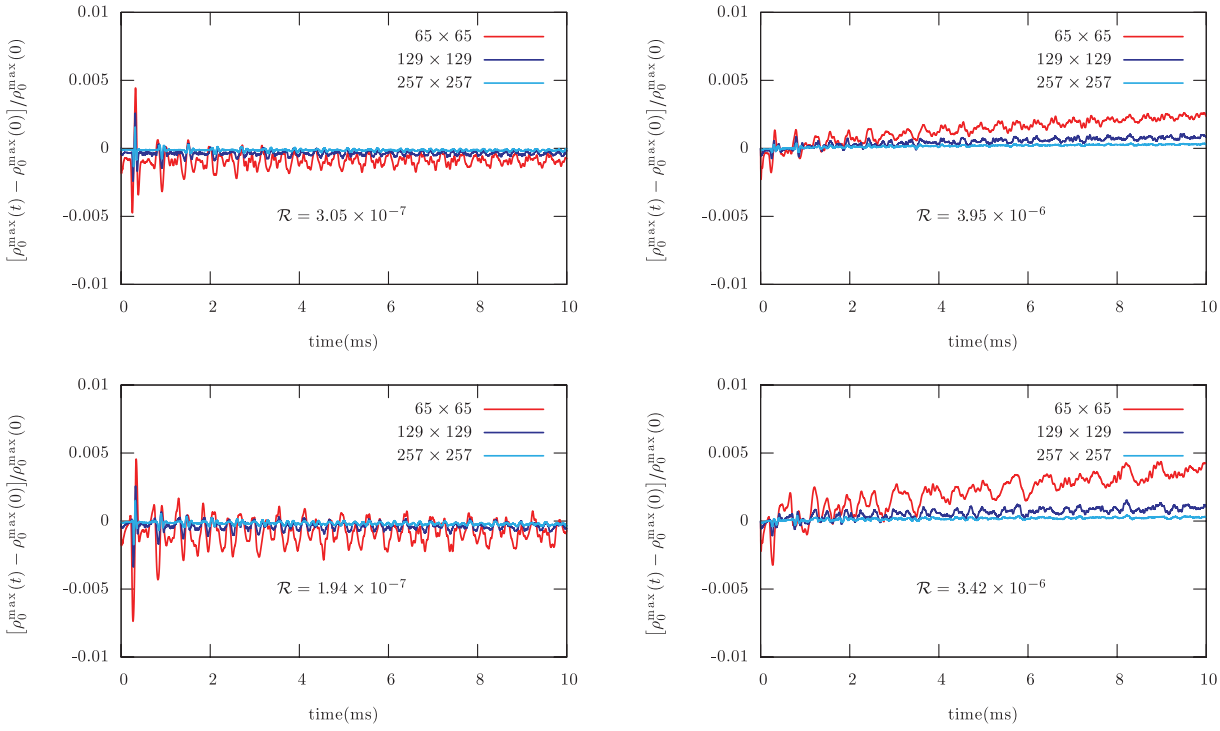

Figure 6. The time-evolution of the maximum rest-mass density changes $\{[\rho_0^{\max}(t) - \rho_0^{\max}(t=0)]/\rho_0^{\max}(t=0)\}$ with different resolutions (65×65: red; 129×129: dark blue; 257×257: sky blue). The upper row shows results when we fix the metric (Cowling approximation), while the lower row shows the case where we consider the fully coupled dynamics. In the left-hand column, we show the figures for a spherical (non-rotating) star, while the right-hand column shows the corresponding figures for a rigidly rotating star with axial ratio = 0.75, which give a rotational frequency of 611 Hz.

It is also very important to check the constancy of the conserved quantities with respect to simulation time. In our formulation, we have two conserved quantities: the total rest mass, M_0, and the total angular momentum, J, which are computed using

$$M_0 = \int D \, \mathrm{d}V^{(3)} = 2\pi \int \frac{\rho_0 W}{(1+2\Phi)^{3/2}} R \, \mathrm{d}R \, \mathrm{d}Z, \tag{25}$$

$$J = \int S_\phi \, \mathrm{d}V^{(3)} = 2\pi \int \frac{\rho_0 h W^2 v^\phi}{(1+2\Phi)^{5/2}} R^3 \, \mathrm{d}R \, \mathrm{d}Z, \tag{26}$$

respectively, and where $\mathrm{d}V^{(3)}$ denotes the three-dimensional volume element. Fig. 7 shows the time-evolution of these two conserved quantities: total rest mass (upper panel) and total angular momentum (lower panel). We show the results only from the rotating star since there is, of course, no angular momentum for non-rotating stars. The deviation of the total rest mass from the initial value has two features: short-term fluctuations and long-term average behaviour. The short-term fluctuations depend on the grid resolution, but the average slopes are almost independent of the resolution. We label the graphs with $\mathcal{R}_M$ and $\mathcal{R}_J$ in a manner analogous to equation (24) and Fig. 6, and use these quantities to measure the long-term stability of the code. Their measured values are consistent with the ones for the central density ($\mathcal{R}$). The behaviour of $\mathcal{R}_M$ is quite similar for the three different grid resolutions, but R_J shows considerable dependence on the grid resolution. We have seen above (see Fig. 6) that the central density fluctuation is significantly dependent on grid resolution only for the rotating models. We conclude that the main reason for this resolution-sensitive behaviour is the

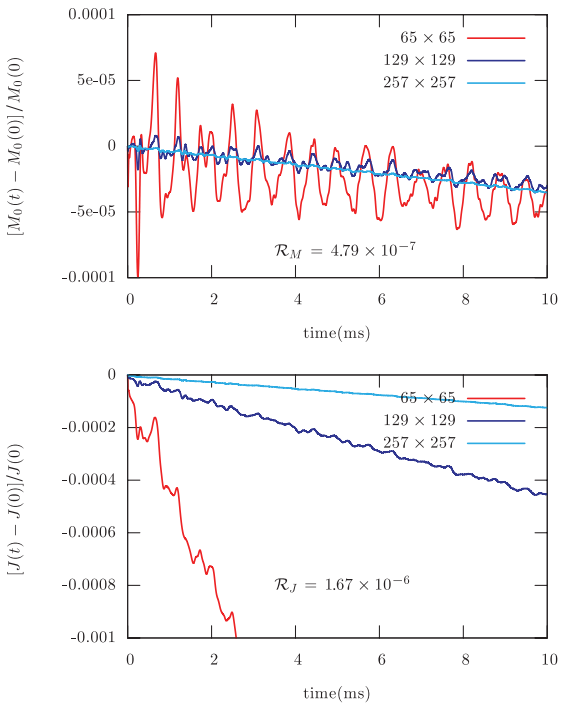

Figure 7. The deviation of total rest mass (upper panel) and angular momentum (lower panel), which should remain constant, from their initial values with time, for the same models as shown in Fig. 6. Results computed with three different resolutions (65×65: red; 129×129: dark blue; 257×257: sky blue) are shown.

fact that angular momentum conservation is sensitive to grid resolution. Therefore, simulations for rotating stars require high grid resolution; otherwise, angular momentum conservation will fail, and other stationary properties of the star (such as central density) will also show substantial, and non-physical, time-evolution.

6 RADIAL PULSATION FREQUENCY TEST

Even without any explicitly added perturbations, it is natural for our numerical simulation of stationary stars to give rise to normal mode oscillations due to intrinsic numerical errors. These errors occur for a variety of reasons, including: (1) the truncation error due to the discretization scheme; (2) the artificial atmosphere (floor) whereby the primitive variables (pressure, density) are restricted from falling below minimum values to avoid code-crashes (the sound velocity becomes unbounded when vacuum is encountered in the numerical calculations); and (3) the numerical limitation in describing the stellar surface. Furthermore, the artificial atmosphere is known to excite higher overtone modes.

The frequencies of various modes depend only on the structure of a given star, and can be calculated by various methods. As explained above, our stationary models oscillate even when we do not explicitly introduce external or internal perturbations. We attempted to compare the frequencies of the modes excited in our models with those obtained by normal mode analysis. The fundamental-mode (F-mode) frequency is very closely related to the dynamical time ($\sim 1/\sqrt{\rho}$) and the associated overtones have frequencies of similar order.

Although using calculations based on cylindrical coordinates is not an efficient way to compute radial pulsations, our code should still be able to approximately compute the correct pulsation frequencies. The detailed perturbation formulations and numerical methods we use for investigating the radial pulsations are described in Appendix A. For initial conditions, we use a non-rotating equilibrium star with a baryon mass $1.4\,\mathrm{M}_\odot$. We performed the test with and without the Cowling approximation, and in order to obtain the mode frequency from the simulations, we analysed the fluctuation of the maximum density with time.

Specifically, we carried out Fourier transformation on the maximum density using the FFTW package (Frigo & Johnson 2005). To obtain better resolution in the frequency domain, we use the zero-padding method which adds additional zeros at the end of the time-series data, effectively using interpolation between points following the basic Fourier transformations. During the process of obtaining a frequency having a maximum sinusoidal amplitude, leakage may also cause additional errors. To reduce the effects of this leakage, we multiply the time-series by a window function. Here we used the Hamming window function defined by

$$w_j = 0.54 + 0.46 \cos\left(\frac{2\pi j}{N}\right), \tag{27}$$

where j is the index of the grid points and N is the total number of points, prior to zero-padding (Harris 1978).

Although, as described above, some modes are excited simply due to numerical error, their amplitudes are too small to be accurately extracted from the simulation. We therefore introduce an explicit perturbation that can more strongly excite the radial modes. The perturbation that we used is

$$\delta\rho_0 = B_\mathrm{s} \sin\left(\pi \frac{r}{r_\mathrm{s}}\right), \tag{28}$$

where B_s is the perturbation amplitude which we set to $B_\mathrm{s} = 0.001$.

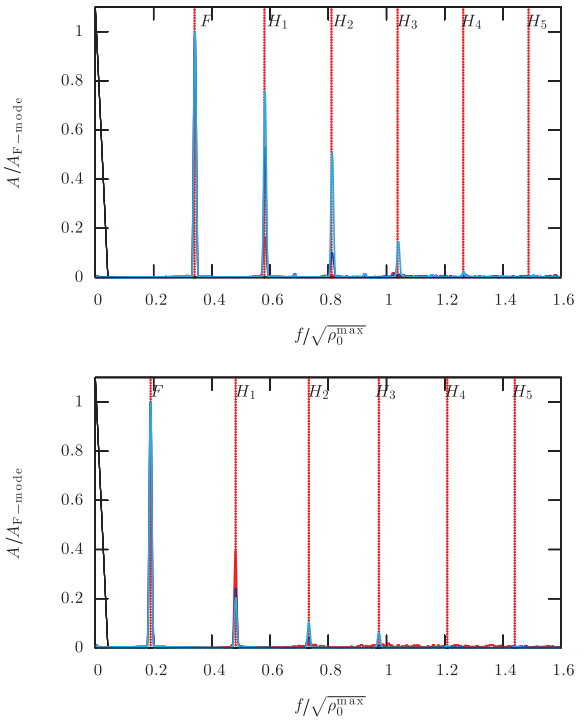

Figure 8. The mode amplitudes of maximum density as a function of frequency of the star with a baryon mass $1.4\,\mathrm{M}_\odot$. The vertical red dotted lines show the frequency of the radial pulsation modes computed using the perturbation method. The top panel shows the result when we use the Cowling approximation, where the gravitational potential is assumed to be fixed. In the bottom figure, we obtain the gravitational potential every few time-steps. In both panels, the three curves show results obtained using three different grid resolutions (sky blue: 257 × 257; dark blue: 129 × 129; red: 65 × 65).

Fig. 8 shows the result after Fourier transformation of the time-series data given by the differences in maximum density relative to the initial time $[\rho_0^{\mathrm{max}}(t) - \rho_0^{\mathrm{max}}(t = 0)]$, and using calculations at different resolutions. For comparison purposes, the vertical red lines show the results computed from linear analysis. The mode labelled as F is the fundamental mode, while H_n denotes the nth overtone radial modes. The results shown in the figure can be summarized as follows:

(i) The most excited mode with the perturbation given by equation (28) is the F mode. By changing the nature of the perturbation, we could make one of the overtones the most highly excited.

(ii) At low resolution, the code cannot identify high-frequency modes. The reason for this is the lack of spatial, not temporal, resolution. The eigenfunctions describing higher overtones have large gradients near the surface which cannot be accurately represented in the low-resolution calculations.

(iii) The frequency increases when we use the Cowling approximation. This is a well-known phenomenon irrespective of whether Newtonian or general relativistic gravitation is used. This issue is discussed in more detail in the appendix.

Table 3 shows the mode frequencies computed from linear analysis as well as the numerical simulations. Again, the stellar model is a non-rotating spherical star of mass $1.4\,\mathrm{M}_\odot$. The relative difference between the linear and full numerical results is listed in the last row. Here the numerical simulations have been carried out using the highest resolution (257 × 257), and we list results computed with and without the Cowling approximation. The frequencies we

Table 3. Comparison of mode frequencies obtained by numerical simulation ($2\pi f$) and by linear analysis (σ).

Mode	F	H_1	H_2	H_3
$f/\sqrt{\rho_0^{\max}}$	0.190	0.482	0.734	0.974
$\sigma/2\pi/\sqrt{\rho_0^{\max}}$	0.190	0.482	0.733	0.974
Error (per cent)	0.000	0.000	0.136	0.000
$\lvert 2\pi f - \sigma\rvert/\sigma$				

obtained from the numerical simulation with 257 × 257 grid resolution have relative differences from those computed from linear analysis of at most 0.1 per cent. We thus conclude that the radial mode frequencies computed from our code agree very well with the ones calculated from linear theory. The largest difference of 0.1 per cent was found in the second overtone (mode H_2), while for other modes we did not find any measurable difference.

7 SUMMARY AND DISCUSSION

We have developed a new hydrodynamical code that adopts a pseudo-Newtonian treatment of the gravitational field. This code uses the so-called 'Valencia formulation' for the hydrodynamical equations. From the computational perspective, the code is modular and includes many reconstruction schemes such as slope limiting techniques (minmod, MC, 3minmod, etc.), PPM and ENO (WENO). In one-dimensional shock tube tests, we assessed code accuracy relative to analytic solutions and computed convergence rates of the errors. We found that the minmod method gives the most diffusive results, smoothing out complex features near discontinuities. As a result it cannot be used to accurately describe stellar surfaces, which are characterized by stiff density changes. The MC method gives the most promising result in the shock tube test and has second-order accuracy. It can capture discontinuities very well in the pulsation mode test, but also yields additional non-physical effects such as the excitation of the higher order overtones near the stellar boundary. The 3minmod and PPM methods can provide higher order accuracy and we have found that they can also describe the stellar surface well.

In the code, we also implemented three different flux approximation schemes: Roe, Marquina and HLLE. Although the results in this paper were all computed using the HLLE approach – which is the most dissipative of the three – we have also found that for the simulations we have considered all produce very similar results.

In the multigrid module for computing the gravitational potential, we have implemented both second- and fourth-order finite-difference discretizations. The actual value of the gravitational potential is slightly different if we change the order of accuracy. However, the changes of maximum density in time show very little sensitivity to the order of approximation, and we consider the difference between the use of the second- or fourth-order method to be insignificant.

In the stationary star test which is described in Section 5, we evolve equilibrium solutions describing both non-rotating and rotating stars using our code. Our code shows stable long-time behaviour of the maximum density and conserved quantities. Based on the rates of change in the maximum density, total mass and total angular momentum, we estimate that our code can be used to study evolution in excess of 3000 dynamical times with 1 per cent error.

In the radial mode test described in Section 6, modes are obtained from the Fourier transformation of the maximum density fluctuations. We also computed normal modes by linear analysis (see Appendix A) and found that the mode frequencies generated by our code agree with the results from linear analysis almost perfectly (less than 0.14 per cent).

This code can be applied to the following astrophysical scenarios:

(i) *Phenomena associated with isolated rotating neutron stars, such as axisymmetric pulsations.* Since our approach can be applied to mildly compact stars, it is very useful to determine the amplitudes and frequencies of the radial and non-radial modes.

(ii) *Core collapses of protoneutron stars.* During these processes, the collapsing fluid velocity can reach up to $\sim 0.2c$, while the gravitational field is relatively weak. Therefore, the pseudo-Newtonian approach is suitable.

(iii) *Accretion discs around a neutron star or black hole.* It is not sufficient to treat a disc around a compact object using Newtonian gravity, since the gravitational field is not weak there. In addition, because the rotational velocity of the disc and the fluid motion of the jet induced by accretion are a significant fraction of c, we should also take into account special relativity in our treatment of hydrodynamics. Our code can be a very good tool for accretion disc studies.

ACKNOWLEDGMENTS

This work was supported by the NRF grant 2006-341-C00018, by NSERC, and by the CIFAR Cosmology and Gravity Program.

REFERENCES

Arnowitt R., Deser S., Misner C. W., 1962, Gravitation: An Introduction to Current Research. Wiley, New York
Brandt A., 1977, Math. Comp., 31, 333
Centrella J. M., Wilson J. R., 1984, ApJS, 54, 229
Colella P., Woodward P. R., 1984, J. Comp. Phys., 54, 174
Cox J. P., 1980, Theory of Stellar Pulsation. Princeton Univ. Press, Princeton, NJ
Donat R., 1998, J. Comp. Phys., 146, 58
Donat R., Marquina A., 1996, J. Comp. Phys., 125, 42
Einfeldt B., 1988, SIAM J. Numer. Anal., 25, 294
Einfeldt B., Roe P. L., Munz C. D., Sjogreen B., 1991, J. Comp. Phys., 92, 273
Font J. A., 2008, Living Rev. Relativ., 11, 7
Font J. A., Miller M., Suen W.-M., Tobias M., 2000, Phys. Rev. D, 61, 044011
Frigo M., Johnson S. G., 2005, Proc. IEEE, 93, 216
Hachisu I., 1986a, ApJS, 61, 479
Hachisu I., 1986b, ApJS, 62, 461
Harris F. J., 1978, Proc. IEEE, 66, 51
Harten A., Lax P. D., van Leer B., 1983, SIAM Rev., 25, 35
Harten A., Engquist B., Osher S., Chakravarthy S. R., 1987, J. Comp. Phys., 71, 231
Jiang G.-S., Shu C.-W., 1996, J. Comp. Phys., 126, 202
Kim J., Kim H. I., Lee H. M., 2009, MNRAS, 399, 229
Liu X.-D., Osher S., Chan T., 1994, J. Comp. Phys., 115, 200
Martí J. M., Müller E., 2003, Living Rev. Relativ., 6, 7
Marti J. M., Ibanez J. M., Miralles J. A., 1991, Phys. Rev. D, 43, 3794
Misner C. W., Thorne K. S., Wheeler J. A., 1973, Gravitation. W. H. Freeman, San Francisco
Nagakura H., Ito H., Kiuchi K., Yamada S., 2011, ApJ, 731, 80
Norman M. L., Winkler K.-H. A., 1986, in Winkler K.-H. A., Norman M. L., eds, NATO Advanced Research Workshop on Astrophysical Radiation Hydrodynamics. Reidel, Dordrecht, p. 449

Roe P. L., 1981, J. Comp. Phys., 43, 357
Roe P. L., 1985, Lect. Notes Appl. Math., 22, 163
Sarbach O., Tiglio M., 2012, preprint (arXiv:1203.6443)
Shibata M., 2003, Phys. Rev. D, 67, 024033
van Leer B., 1977, J. Comp. Phys., 23, 276
van Leer B., 1979, J. Comp. Phys., 32, 101
Wilson J. R., 1972, ApJ, 173, 431
Wilson J. R., Mathews G. J., 2003, Relativistic Numerical Hydrodynamics. Cambridge Univ. Press, Cambridge
Zhang W., MacFadyen A. I., 2006, ApJS, 164, 255

APPENDIX A: PERTURBATION EQUATION

The eigenfrequencies and eigenfunctions of the radial pulsation of stars are well known in Newtonian hydrodynamics as well as in the general relativistic case. However, the corresponding formulation has not been previously presented for our pseudo-Newtonian approach. Here, we describe the linearized equations that can be used to obtain eigenfrequencies and eigenfunctions of the normal modes of spherical stars using this approximation, and following the general relativistic framework described in Misner, Thorne & Wheeler 1973 (hereafter MTW). First, to describe stellar oscillations – such as those occurring on the surface – it is much more practical to use a Lagrangian description rather than the Eulerian one adopted in Section 2. The relation between the Eulerian and Lagrangian perturbations is (see e.g. Cox 1980)

$$\Delta f(t,r) = \delta f + f_0'\zeta, \tag{A1}$$

where ζ is a Lagrangian variation in space. The law of baryon number conservation $[\nabla_\mu(nu^\mu) = 0]$ gives

$$\Delta n = -n_0\left[r^{-2}\alpha_0^3\left(r^2\alpha_0^{-3}\zeta\right)' - 3\alpha_0^{-1}\delta\alpha\right], \tag{A2}$$

where $\alpha = \sqrt{1+2\Phi}$, n is the baryon number density and $'$ denotes differentiation with respect to r (see equation 26.7 in MTW). The relation between n in equation (A2) and ρ_0 is $\rho_0 = m_\mathrm{b}n$, where m_b is baryon mass and the subscript 0 denotes the unperturbed state.

Another perturbation equation comes from the adiabatic EoS which offers a much easier way to find the pressure variation:

$$\Gamma = \frac{n}{P}\frac{\mathrm{d}P}{\mathrm{d}n}. \tag{A3}$$

Since the Lagrangian variations commute with total differentiation (denoted by 'd'), equation (A3) becomes

$$\Gamma = \frac{n}{P}\frac{\Delta P}{\Delta n}. \tag{A4}$$

In addition, equations (A1), (A2) and (A4) give the following pressure variation equation:

$$\delta P = -\Gamma P_0\left[r^{-2}\alpha_0^3(r^2\alpha_0^{-3}\zeta)' - 3\alpha_0^{-1}\delta\alpha\right] - \zeta P_0'. \tag{A5}$$

The energy conservation equation ($u_\mu\nabla_\nu T^{\mu\nu}$) gives

$$\Delta\rho = \frac{\rho_0 + P_0}{n_0}\Delta n. \tag{A6}$$

Note that ρ_0 is the energy density in the unperturbed state, rather than the rest-mass density used in the main text. Combining this with equation (A2), we obtain the equation for the energy density variation

$$\delta\rho = -(\rho_0 + P_0)\left[r^{-2}\alpha_0^3(r^2\alpha_0^{-3}\zeta)' - 3\alpha_0^{-1}\delta\alpha\right] - \zeta\rho_0'. \tag{A7}$$

The main difference here relative to the general relativistic case arises in the computation of the perturbation of the gravitational potential. The Poisson equation gives

$$\frac{2}{r}(\alpha_0\delta\alpha)' + (\alpha_0\delta\alpha)'' = 4\pi(\delta\rho + 3\delta P). \tag{A8}$$

Note that we should use only the Eulerian variation in this equation since Lagrangian variation does not commute with partial differentiation. Equation (26.16) in MTW involves only first-order differential equations, that is, the second-order differentiations are rewritten in terms of the first-order differentiations. On the other hand, in our case, we cannot find any equations that can be used to eliminate the second-order differentiation. That means we need to find one more boundary condition to solve this equation.

Finally, the equation of motion of the fluid is obtained from the 4-acceleration ($a_\mu = u^\nu\nabla_\nu u_\mu$)

$$(\rho_0 + P_0)\alpha_0^{-4}\ddot{\zeta} = -\delta P' - (\delta\rho + \delta P)\alpha_0^{-1}\alpha_0' - (\rho_0 + P_0)\left(\alpha_0^{-1}\delta\alpha' - \alpha_0^{-2}\alpha_0'\delta\alpha\right). \tag{A9}$$

Under the assumption of the adiabatic nature of the oscillation, normal modes are standing waves, and thus space and time variables can be separated as follows:

$$\zeta(r,t) = \xi(r)\mathrm{e}^{\mathrm{i}\sigma t}. \tag{A10}$$

Then, we can rewrite the equations A5, A7 and A9 using ξ and σ,

$$\delta P = -\Gamma P_0\left[r^{-2}\alpha_0^3(r^2\alpha_0^{-3}\xi)' - 3\alpha_0^{-1}\delta\alpha\right] - \xi P_0', \tag{A11}$$

$$\delta\rho = -(\rho_0 + P_0)\left[r^{-2}\alpha_0^3(r^2\alpha_0^{-3}\xi)' - 3\alpha_0^{-1}\delta\alpha\right] - \xi\rho_0', \tag{A12}$$

$$(\rho_0 + P_0)\alpha_0^{-4}\sigma^2\zeta = \delta P' + (\delta\rho + \delta P)\alpha_0^{-1}\alpha_0' + (\rho_0 + P_0)\left(\alpha_0^{-1}\delta\alpha' - \alpha_0^{-2}\alpha_0'\delta\alpha\right). \tag{A13}$$

To solve equations (A11)–(A13), we need to impose appropriate boundary conditions. The first condition is that ξ/r should be regular at the origin, and the second one is that the pressure variation at the surface must vanish, that is,

$$\frac{\xi}{r} = \text{finite at } r = 0, \tag{A14}$$

$$\Delta P(r = r_\mathrm{s}) = 0. \tag{A15}$$

Unlike the general relativistic case, we cannot substitute $\delta\alpha$ and $\delta\alpha'$ with other variations such as $\delta\rho$ and δP. Therefore, we need an additional boundary condition for equation (A8). We use the properties of the gravitational potential to obtain extra conditions. First, from the condition that the gravitational potential should be regular at the centre, we obtain

$$\delta\alpha' = 0 \quad \text{at} \quad r = 0. \tag{A16}$$

Secondly, because the gravitational potential should fall off as $1/r$ beyond the stellar surface, we have

$$\delta\Phi' + \frac{\delta\Phi}{r} = 0. \tag{A17}$$

When we apply the above equation at the stellar boundary ($r = r_\mathrm{s}$), we get

$$\delta\alpha' = -\frac{\delta\alpha^2 - 1}{2r\delta\alpha} \quad \text{at} \quad r = r_\mathrm{s}. \tag{A18}$$

Since equations (A11)–(A13) and (A8) are coupled, we use an iterative method to solve them.

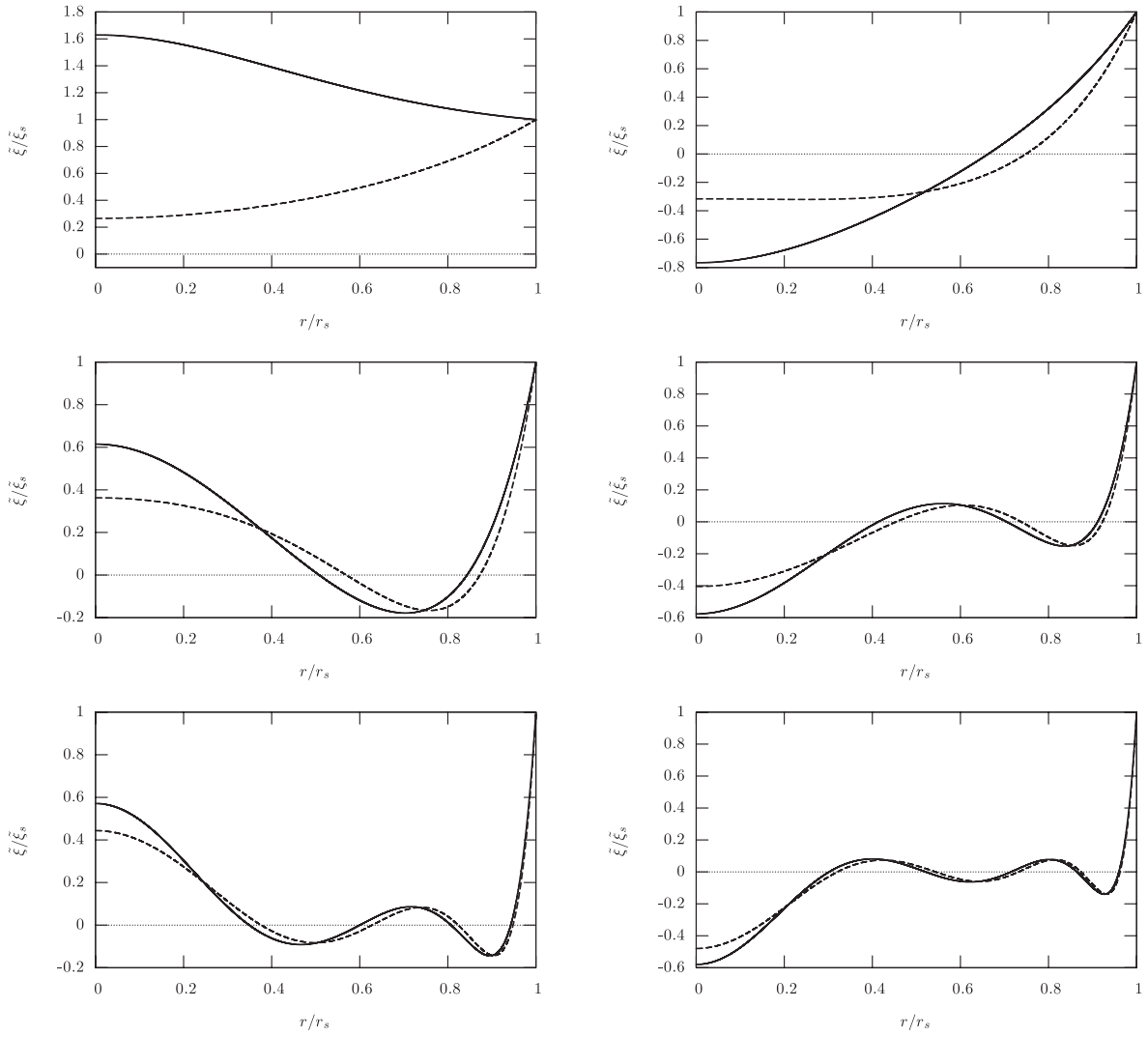

Figure A1. Radial pulsation eigenfunction of a 1.4-$M_\odot$ star. The EoS that we use is a polytropic one with $K = 100$ and $N = 1$. In this figure, $\tilde{\xi} = \xi/r$ and $\tilde{\xi}_s = \tilde{\xi}(r = r_s)$, where r_s is the surface radius. The dashed and solid lines represent the results with and without the Cowling approximation, respectively. Each panel shows different modes [top left-hand panel: (F); top right-hand panel: (H_1); middle left-hand panel: (H_2); middle right-hand panel: (H_3); bottom left-hand panel: (H_4); and bottom right-hand panel: (H_5)] which have different oscillation frequencies.

For the case of the Cowling approximation, which assumes that the gravitational potential is fixed ($\delta\alpha = 0$), the equations simplify considerably:

$$\delta P = -\Gamma P_0 \left[r^{-2}\alpha_0^3 (r^2\alpha_0^{-3}\xi)' \right] - \xi P_0', \tag{A19}$$

$$\delta\rho = -(\rho_0 + P_0) \left[r^{-2}\alpha_0^3 (r^2\alpha_0^{-3}\xi)' \right] - \xi\rho_0', \tag{A20}$$

$$(\rho_0 + P_0)\alpha_0^{-4}\sigma^2\zeta = \delta P' + (\delta\rho + \delta P)\alpha_0^{-1}\alpha_0'. \tag{A21}$$

If we compare the above equations with equations (A11)–(A13), we observe that every coefficient of $\delta\alpha$ is negative: therefore, as mentioned in the main text, σ increases when we apply the Cowling approximation.

We show the solution for ξ/r for the 1.4-$M_\odot$ star with $K = 100$ and $N = 1$ with and without the Cowling approximation in Fig. A1. The σ values corresponding to each mode are summarized in Table 3 which appears in the main text.

This paper has been typeset from a TEX/LATEX file prepared by the author.